UC Irvine
UC Irvine Previously Published Works

Title
The influence of liquid-state multifrequency ultrasonic treatment on the microstructure and solidification chronology of A380 aluminum alloy

Permalink
https://escholarship.org/uc/item/0q3348pj

Journal
Materials Science and Engineering A, 977

ISSN
0921-5093

Authors
Jaime, Raquel F
Zang, Andrew Y
Chang, Adrianne
et al.

Publication Date
2026-12-01

DOI
10.1016/j.msea.2026.151104

Copyright Information
This work is made available under the terms of a Creative Commons Attribution-NoDerivatives License, available at https://creativecommons.org/licenses/by-nd/4.0/

Peer reviewed

eScholarship.org Powered by the California Digital Library
University of California

Materials Science & Engineering A 977 (2026) 151104

Contents lists available at ScienceDirect

Materials Science & Engineering A

journal homepage: www.elsevier.com/locate/msea

The influence of liquid-state multifrequency ultrasonic treatment on the microstructure and solidification chronology of A380 aluminum alloy

Raquel F. Jaime [a], Andrew Y. Zang [a,b], Adrianne Chang [a], Carl Söderhjelm [a], Hélder Puga [a,c], Diran Apelian [a,b,*]

[a] Advanced Casting Research Center (ACRC), University of California, Irvine (UCI), Irvine, CA, 92697, USA
[b] Pratt & Whitney Center for Solidification Science, UCI, Irvine, CA, 92697, USA
[c] CMEMS, University of Minho, Guimarães, Portugal

ARTICLE INFO

Keywords:
A380 aluminum alloy
Ultrasonic treatment
Fe-rich intermetallics
Heterogeneous nucleation
Solidification sequence
Grain refinement
AlP

ABSTRACT

Liquid-state Ultrasonic Treatment (UST) is an emerging industrial liquid-processing method to enhance the quality and microstructure of cast parts while eliminating the need for chemical modifiers. The effects of liquid-state UST on the solidification chronology, grain refinement, and the morphology of secondary phases of commercial A380 aluminum alloy are systematically investigated to identify the limiting processing conditions and elucidate the underlying mechanisms. Multifrequency Multimode Modulated (*mf*-UST) is a novel impartment method that eliminates intensity decay via frequency-swept ultrasonics. Trials were completed in commercial A380 aluminum alloy using *mf*-UST impartment method above the liquidus temperature. A380 was chosen to observe the effectiveness of treatment on the modification of Fe-containing intermetallics such as β-Al_5FeSi and α-$Al_{15}(Fe, Mn)_3Si_2$ which appear frequently in recycled aluminum compositions. Samples were produced from trials at three treatment temperatures (700 °C, 680 °C, 660 °C) and three treatment times (5, 10, 15 min). Liquid state *mf*-UST modified the formation and morphology of the α-$Al_{15}(Fe, Mn)_3Si_2$ intermetallic phase and could be tailored via changing treatment time. *mf*-UST provoked the production of an unusually stable modified Si within the hypoeutectic alloy which nucleates on AlP and AlP/cavity combinations. The maximum observed grain refinement was found within 5 min of *mf*-UST at 680 °C displaying an 85.8% reduction in grain size. Results demonstrate that *mf*-UST applied in the liquid state influences solidification chronology and thus impacts the resultant intermetallic morphology. These new primary intermetallic morphologies likely affect the degree of Al grain refinement, in addition to the pre-existing 'oxide refinement' theory.

1. Introduction

The production of primary aluminum (Al) from bauxite ore is an environmentally taxing process, responsible for the emission of more than 1.2 billion tons of CO_2 annually with each tonne of Al producing approximately 2 tonnes of CO_2 [1]. This value will increase due to the demand for aluminum; concomitantly, the number of ethical sources of bauxite in the world remains limited [2]. Given these limitations and ethical responsibilities, we need to prioritize secondary sources of Al and increase recycling rates of end of life (EoL) Al components. A major challenge to the utilization of recycled Al alloys is the contamination that results in an out-of-spec composition. This is mitigated with the use of new scrap from controlled sources; however, old scrap contains a mixed variety of alloys which often leads to contamination. As an example, elevated Fe content in an A380 alloy is commonly treated through the addition of Mn which transforms the detrimental Fe-intermetallics (i.e., β-Al_5FeSi) to α-$Al_{15}(Fe, Mn)_3Si_2$ [3,4]. UST offers a sustainable liquid processing method to treat secondary aluminum alloys without the addition of chemical additives, modifying the subsequent microstructure via intermetallic phase morphology and grain refinement for use in high integrity applications [5–8].

Ultrasonic melt treatment influences liquid metals primarily through acoustic cavitation and acoustic streaming. Cavitation promotes the activation, fragmentation and redistribution of non-metallic inclusions, whereas streaming enhances bulk transport for thermal and compositional homogenization [5,9–11]. The relative contribution of these mechanisms depends on the acoustic field, melt properties, temperature, gas content and treatment geometry. Conventional UST equipment

* Corresponding author. Advanced Casting Research Center (ACRC), University of California, Irvine (UCI), Irvine, CA, 92697, USA.
E-mail address: dapelian@uci.edu (D. Apelian).

https://doi.org/10.1016/j.msea.2026.151104
Received 2 September 2026; Received in revised form 14 September 2026; Accepted 16 September 2026
Available online 17 September 2026
0921-5093/© 2026 The Authors. Published by Elsevier B.V. This is an open access article under the CC BY license (http://creativecommons.org/licenses/by/4.0/).

functions on a fixed frequency, however, multifrequency multimode modulated ultrasonics (*mf*-UST) is a novel impartment method which employs one system sweeping across multiple frequencies to mitigate amplitude decay [8]. The benefit of multifrequency is that frequency sweeping reduces sensitivity to resonance detuning caused by changes in melt temperature, immersion conditions and acoustic loading, thereby helping to sustain energy transmission during treatment [12–16].

The phenomenon of dendrite fragmentation resulting from combined UST mechanisms of acoustic cavitation and streaming during solidification has been well studied [17,18]. However, the application of *mf*-UST as a liquid metal processing method to modify the resultant solidified structure and properties, especially when applied to secondary Al production has much value and requires further investigation [19–21]. For *mf*-UST applied above the liquidus temperature, oxides and other solid contaminants that exist within the melt are fragmented and distributed by sonification. These particles may then act as sites for nucleation of α-Al grains, thus refining the grain structure [22,23]. Discerning alternative mechanisms of *mf*-UST grain refinement aside from oxide refinement facilitates greater use of *mf*-UST processing. Liquid-state *mf*-UST has also been shown to modify intermetallic phases in the final casting, yet there is limited understanding of the mechanisms involved. As such, fully understanding the mechanisms of liquid-state *mf*-UST grain refinement and intermetallic modification is needed for industrial viability and adoption.

Liquid-state *mf*-UST has potential for a multifaceted treatment method to refine and enhance cast alloys as an all-in-one molten metal processing step. This study tests the hypothesis that *mf*-UST above the liquidus modifies the activation and spatial distribution of heterogeneous nucleation substrates, thereby altering the phases formed during subsequent solidification. The experimental parameters of treatment temperature and time are systematically varied to investigate the underlying mechanisms. A380 was chosen specifically to view the impact of *mf*-UST on the α-$Al_{15}(Fe, Mn)_3Si_2$ intermetallic phase which is detrimental to the mechanical properties of A380 as well as many secondary Al-Si alloys contaminated with high Fe [3,24,25]. This study shows that liquid-state *mf*-UST alters the solidification chronology of the A380 alloy, resulting in the production of blocky-Si and polyhedral Fe-intermetallic phases which do not form in the non-treated material. We found evidence that these new phase formations are the result of three factors: 1) break-up of potent nucleants; 2) local *mf*-UST induced chemical heterogeneity; and 3) cavitation undercooling. The results of this study indicate that solid oxides and phosphides are fragmented and dispersed by *mf*-UST, after which they act as nucleation sites for cavitation bubbles to develop and/or primary phase nucleation. These favorable nucleation sites accompanied with local induced hypereutectic regions result in an altered solidification chronology with unexpected primary phase formation. These new faceted primary phases provide heterogeneous nucleation sites for Al grains in addition to fragmented and dispersed oxides.

2. Materials and methods

2.1. Materials, ultrasonic treatment, and casting

Commercial Al A380 was used in this study, and its measured average chemical composition across all the experimental work is listed in Table 1. As noted, the alloy contains 0.2 wt% content of Mn which is theoretically not enough to convert β-Al5FeSi into the α-$Al_{15}(Fe, Mn)_3Si_2$ intermetallic phase [3]. A380 was selected for this study because of the exaggerated nature of its microstructure, with intermetallic and eutectic features on the scale of 10-20 μm in length. Features of this scale are ideal for visualizing and identifying the fundamental mechanisms of liquid-state *mf*-UST processing. The Scheil solidification curve of A380 was calculated using Thermo-Calc CALPHAD to determine the predicted solidification chronology in absence of ultrasonic processing.

For each trial, 10 kgs of commercial A380 ingots were melted in an induction tilt furnace with an inner diameter of 14 cm and depth of 33 cm (Fig. 1(a)). The ultrasonic probe was preheated before immersing into the center of the melt to a depth of approximately 10 cm. An MPI 2000 Ultrasonic Sonorod Generator produced a power output in the range of 800-1000 W [26]. The driving frequency was set in the range of 19.5 kHz to 21.5 kHz, to maintain resonance with the melt volume, and transmitted along a waveguide to an 8 cm outer diameter hollow SiAlON probe (Fig. 1(a)). Treatment was applied in a pulsed impartment mode, with a cycle of 5 s of *mf*-UST on, followed by 2 s off for the duration of the treatment time. The pulsed regime was selected to limit continuous acoustic shielding and excessive thermal loading of the probe. No direct measurement of cavitation persistence during the off period was performed. *mf*-UST was conducted isothermally, i.e. treatment temperature and casting temperature are the same for each respective trial. After *mf*-UST, the probe was removed, and a preheated ladle was submerged ~10 cm deep into the melt for all sample collection.

Table 2 shows the samples collected from trials at three processing temperatures, 700 °C, 680 °C, and 660 °C across different treatment times, 0 min (untreated), 5 min, 10 min, and 15 min. For untreated sample collection, commercially produced A380 ingots were melted and held at the respective temperature, then an untreated sample was collected via pre-heated ladle and poured into a steel mold held at 110 °C as well as into the thermal analysis instrument (Fig. 1(c and d)). After untreated sample collection for all temperatures considered, *mf*-UST was applied isothermally to the same metal bath (1 bath per temperature) for a 5 min treatment followed by casting into the steel mold and obtaining a thermal analysis sample. For 10- and 15-min treatments at all temperatures, a separate melt was conducted, and a steel mold casting was collected. Each trial was repeated for fidelity in results. To investigate the effects of *mf*-UST on the local alloying element concentrations, an additional sample was collected at a significantly increased cooling rate, i.e. supercooled in water at a cooling rate of approximately 100 °C/s for samples treated with 5 min of *mf*-UST.

2.2. Characterization

The untreated material was prepared and characterized with a Spectro Lab LAS01 optical emission spectroscopy (OES) for compositional analyses. Castings made in the steel molds were all cross-sectioned 2 cm from the bottom of the casting (Fig. 1(c)). Cross-sections were polished to a mirror finish with colloidal silica as the final step. After polishing, the surfaces were argon-etched via GATAN PECS II at 8 keV and 4 keV with a 4°-gun angle for 20 min total. Select samples were etched with 1M NaOH for 10 min to reveal phase morphology. Cross-sections were viewed in an Evident Scientific DSX10-UZH optical microscope (OM) to image the microstructure of both untreated and *mf*-UST samples from all trials. A TESCAN-GAIA3 field emission scanning electron microscope (FE-SEM) was used to further analyze the microstructures and obtain relative compositional data through Oxford Instruments energy dispersive x-ray spectroscopy (EDS) for phase analysis and electron backscatter diffraction (EBSD) for grain size analysis.

Table 1
Average chemical composition and standard deviation of commercial aluminum A380 alloy via OES (wt.%).

	Si	Cu	Zn	Fe	Mn	Mg	Cr	Ti	Na	P	Sr	B
A380	8.38	3.64	2.30	0.859	0.201	0.081	0.071	0.041	0.002	0.001	-	-
SD	*0.112*	*0.102*	*0.025*	*0.020*	*0.004*	*0.001*	*0.003*	*0.009*	*0.0003*	*0.0002*	-	-

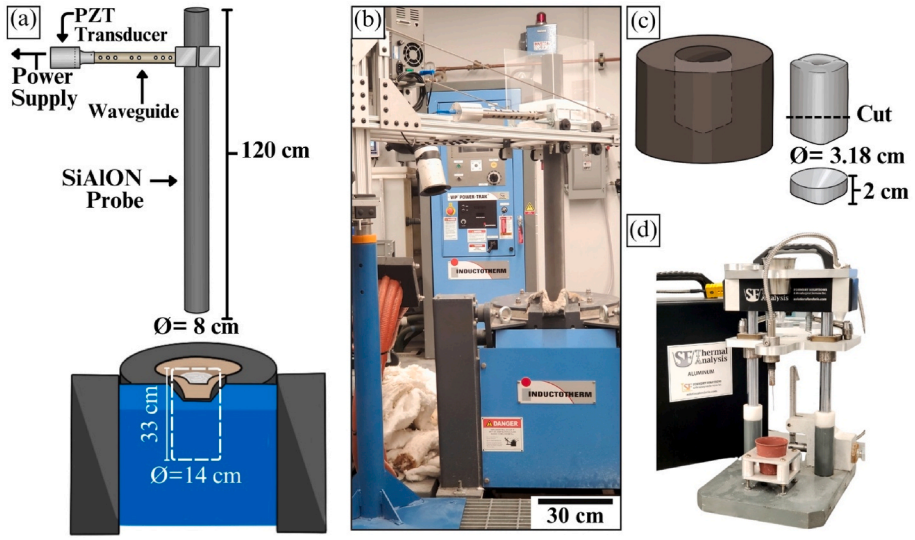


Fig. 1. (a) Schematic of the multifrequency ultrasonic equipment components and dimensions of the 10 kg capacity induction furnace, (b) image of experimental setup, (c) steel mold and casting cross-section for microstructure characterization, (d) thermal analysis equipment.

Table 2
Processing and casting parameters for steel mold and thermal analysis sample collection.

mf-UST Casting Temperature	*mf*-UST Time			
	0 min (Untreated)	5 min	10 min	15 min
700 °C	✓*	✓*	✓	✓
680 °C	✓*	✓*	✓	✓
660 °C	✓*	✓*	✓	✓

✓ = Steel Mold Casting * = Thermal Analysis Sample.

Focused ion beam (FIB) serial sectioning was performed on a FEI Quanta 3D FEG dual beam SEM/FIB using a nominal slice thickness of 100 nm and a 7 nA ion beam cutting current. Average grain size was calculated from collected SEM-EBSD patterns using ImageJ and via measurement of the average Feret diameter. Average intermetallic area and area fraction were calculated using ImageJ on 13 SEM-EDS maps of the microstructure taken with the same 280 μm horizontal field width.

3. Results

3.1. Al grains

Fig. 2 shows EBSD patterns of all collected steel mold samples. All EBSD patterns were collected from the center of the cross-sectioned sample at the same depth within the sample (Fig. 1(c)). Average grain size values for all samples are summarized in Table 3 and in the surface plot in Fig. 3. The observed grain refinement is evident between untreated samples and those treated at 5 min of *mf*-UST for temperatures of 680 °C and 660 °C. These samples experienced an initial decrease of 85.8% and 77.4%, respectively. Meanwhile, the 700 °C experienced an initial decrease of only 11.2% and continued to decrease with additional treatment time. For 680 °C and 660 °C samples treated with 10 and 15 min of *mf*-UST the average grain size remains lower than the untreated sample. Interestingly, at 10 min of treatment both samples have a minor increase in grain size followed by a minor decrease with 15 min of treatment.

3.2. Modified phases

Fig. 4 shows OM images of the untreated and *mf*-UST microstructures for each treatment temperature and processing time. The untreated microstructures of all treatment temperatures, first column, depict the morphologies for primary Al, α-$Al_{15}(Fe, Mn)_3Si_2$, Si eutectic, and Al_2Cu phases. Beginning with samples treated with UST for 5 min, new phase morphologies appear. At all treatment temperatures a block-like faceted phase appears, and at 680 °C and 660 °C a star-like phase also appears, confirmed via SEM-EDS as Si and polyhedral Fe-intermetallic phases, respectively (Fig. 5) [27–29]. In *mf*-UST samples with polyhedral Fe-intermetallic, this phase is surrounded by networks of Fe-containing branches that extend from the peaks of the star-like shape in a star-burst pattern. Al_2Cu is commonly seen attached to the extrusions of the polyhedral Fe-intermetallic, as shown in the SEM-EDS of Fig. 5. Surrounding blocky-Si are branches of Si eutectic in a similar star-burst pattern observed with the polyhedral Fe-intermetallic. Majority of these blocky-Si phases contain a 'pore' near the center in the cross-section, which is of interest, and will be further discussed below. There are no major changes to the Si eutectic nor the Al_2Cu phase with *mf*-UST.

The size and amount of both modified Si and polyhedral Fe-intermetallic within the *mf*-UST samples is dependent on treatment conditions. Fig. 6 shows the variations in average area and area fraction of modified intermetallic phases for all *mf*-UST processed conditions. These values were obtained by collecting 13 EDS maps of identical 280 μm view field for each sample condition. ImageJ was used to isolate the areas of modified Si and polyhedral Fe-intermetallic, shown with standard deviation values for each condition (Fig. 6(a)). Those averages were then divided by the total area collected in the 13 maps for area fraction (Fig. 6(b)).

Blocky-Si forms in all samples treated with *mf*-UST. However, polyhedral Fe-intermetallic does not form in any metal processed at 700 °C. In samples treated at 680 °C and 660 °C an interesting pattern occurs. After 5 min of *mf*-UST, polyhedral Fe-intermetallic forms, however this phase disappears after 10 min of treatment, and in the case of the sample treated at 660 °C the phase reappears after 15 min. The polyhedral Fe-rich morphology was not detected in the microstructure nor the thermal analysis data of any samples treated at 700 °C Polyhedral Fe-intermetallic is temperature sensitive and does not form at any treatment/casting temperature higher than 680 °C.

The three samples with the smallest grain sizes, 680 °C with 5 min of *mf*-UST, 660 °C with 5 and 15 min of *mf*-UST (110 μm, 180 μm, 173 μm, respectively, Fig. 3) displayed a combination of both relatively low modified Si average areas/area fractions, and the presence of the polyhedral Fe-intermetallic phase morphology. Considering the 660 °C

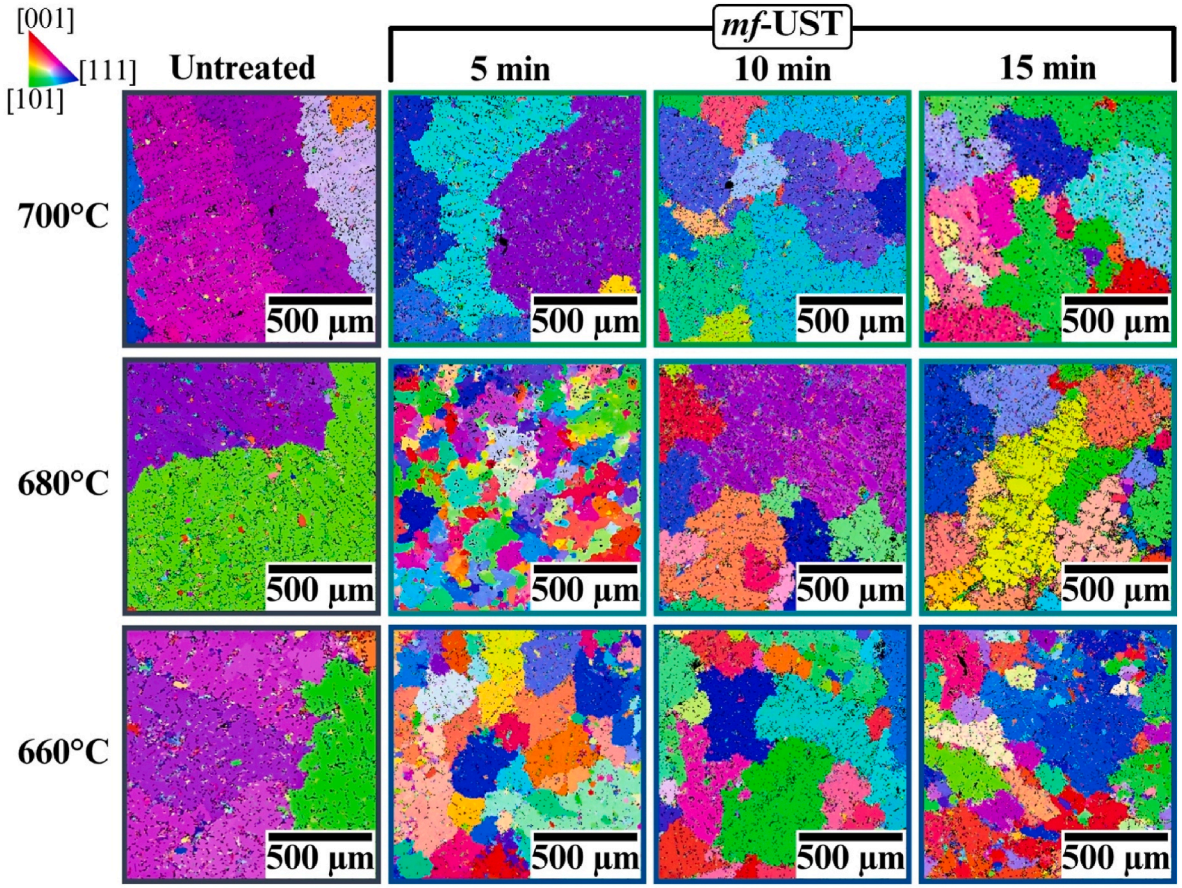


Fig. 2. Map of SEM-EBSD patterns of A380 samples at three processing temperatures across different treatment durations. *Rows from top to bottom:* 700 °C, 680 °C, and 660 °C. *Columns from left to right:* untreated reference, 5 min treatment, 10 min treatment, and 15 min treatment. Scale bar = 500 μm.

Table 3
Average grain size values for all samples in μm with standard deviation.

mf-UST Casting Temperature	*mf*-UST Time			
	0 min (Untreated)	5 min	10 min	15 min
700 °C	776 ± 442 μm	689 ± 245 μm	394 ± 228 μm	351 ± 193 μm
680 °C	781 ± 448 μm	110 ± ..71 μm	395 ± 297 μm	289 ± 232 μm
660 °C	769 ± 453 μm	180 ± 104 μm	296 ± 186 μm	173 ± 119 μm

samples, there is a fluctuation in the achievable grain refinement of these samples with average grain sizes of 180 μm to 296 μm to 173 μm with 5, 10, and 15 min of *mf*-UST accordingly. In accordance with this fluctuation in grain size, there is a fluctuation in the Fe-containing phase morphology. Fig. 7(a, b) shows optical micrographs of the variations seen in Fe-phase morphology across all treatment conditions. All samples, untreated or treated across all conditions contain the script-like Fe-phase morphology known commonly as α-Al_{15}(Fe, Mn)$_3Si_2$ [24,25,30]. However, in samples *mf*-UST processed for 5 min at 680 °C and 660 °C, the polyhedral Fe-intermetallic morphology appears alongside the α-Al_{15}(Fe, Mn)$_3Si_2$. Interestingly, in these samples we observe the lowest average grain sizes. At 10 min of *mf*-UST processing, the polyhedral Fe-intermetallic is absent and replaced with a needle-like morphology reminiscent of the β-Al_5FeSi phase for all treatment temperatures, which is simultaneous with an increase in grain size for 680 °C and 660 °C. After 15 min of *mf*-UST processing, the polyhedral Fe-intermetallic re-emerges in the 660 °C case only. The samples processed at 700 °C and 680 °C revert to only the α-Al_{15}(Fe, Mn)$_3Si_2$. In summary, all samples alternate their morphology from script or script/polyhedral Fe-intermetallic, to script and needle-like, and back to script or script/polyhedral Fe-intermetallic (Fig. 7(a, b)). This fluctuation is reflected in the grain refinement seen Fig. 3 where the achievable grain size coincides with the morphology of the Fe-intermetallic.

3.3. Particles within modified Si and Fe-rich phases

In the *mf*-UST processed samples, one of the most notable features regarding modified Si is the frequently observed 'pore' at the cross-sectioned surface, Fig. 7(c). This 'pore' is approximately 1 μm in diameter, commonly near the center of the cross-sectioned modified Si. To eliminate sample preparation effects which have the potential to dissolve/remove solid particles that may have been present in revealed pores, SEM-EDS was used to search for subsurface EDS signals within the modified Si particles. Fig. 8(a) shows SEM-EDS maps of an example of a Si phase without an exposed pore on the surface, however, with a clear signal below the surface for aluminum and phosphor. SEM-FIB serial sectioning was performed of this location to excavate the particle trapped within. Fig. 8(b, c) reveals a particle of AlP and not a pore. It is likely that AlP was removed from the sample during sectioning and polishing procedures leaving behind the pores typically seen on the phase

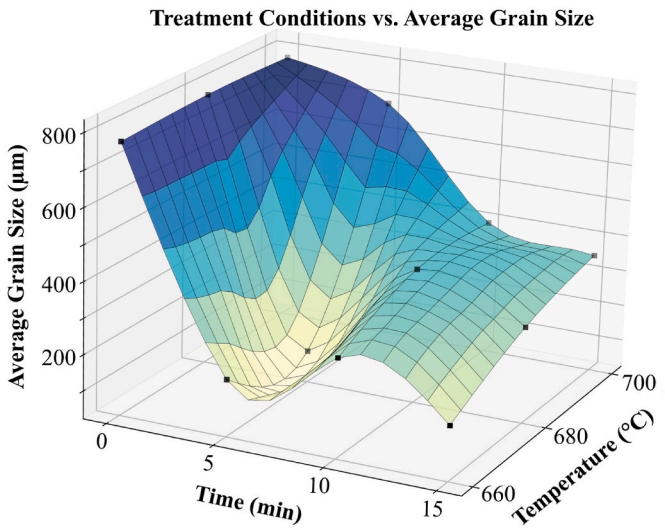


Fig. 3. 3D interpolated surface plot of average grain size vs. treatment temperature and treatment time.

surfaces. Supplemental serial sectioning and FIB erosion of the surface of additional Si particles reveal that in some cases, an attached pore is also observed alongside the AlP particle (Fig. 9). Modified Si appears to be a permanent artifact of *mf*-UST. When samples treated with *mf*-UST were cast, remelted, and cast subsequently without *mf*-UST, modified Si was observed in the microstructure (Fig. 10). Minor grain refinement is observed in the material as the grain size did not revert to what was seen in the untreated samples.

In less frequent cross-sections a similar pore can be found in the polyhedral Fe-intermetallic phase, an example is shown in Fig. 7(b) for the sample treated at 660 °C. This pore indicates a nucleating particle that was likely removed during metallography. Due to the relatively large scale of this phase when compared to modified Si, the probability of encountering a pore at the cross-section or near the surface via EDS signal is much lower. To overcome this, FIB was used on many polyhedral Fe-phases to erode the surface layer by layer until a particle was reached. Fig. 8(d) shows an example of a particle and the respective EDS identification. Overall, the particles from within polyhedral Fe-phase displayed signals of Ti and O. The exact ratio cannot be definitively determined via SEM-EDS alone.

3.4. Thermodynamic simulation & thermal analysis

Thermo-Calc software was used to produce the nonequilibrium Scheil solidification curve of A380 in the untreated condition with the average composition (Table 1, Fig. 11). According to the Scheil solidification curve of untreated A380, the primary Al matrix grows first at the liquidus temperature of 585 °C, followed by the formation of the β-Al_5FeSi phase which solidifies at approximately 0.012 mass fraction solid. Eutectic Si begins to form at approximately 0.3 mass fraction solid,

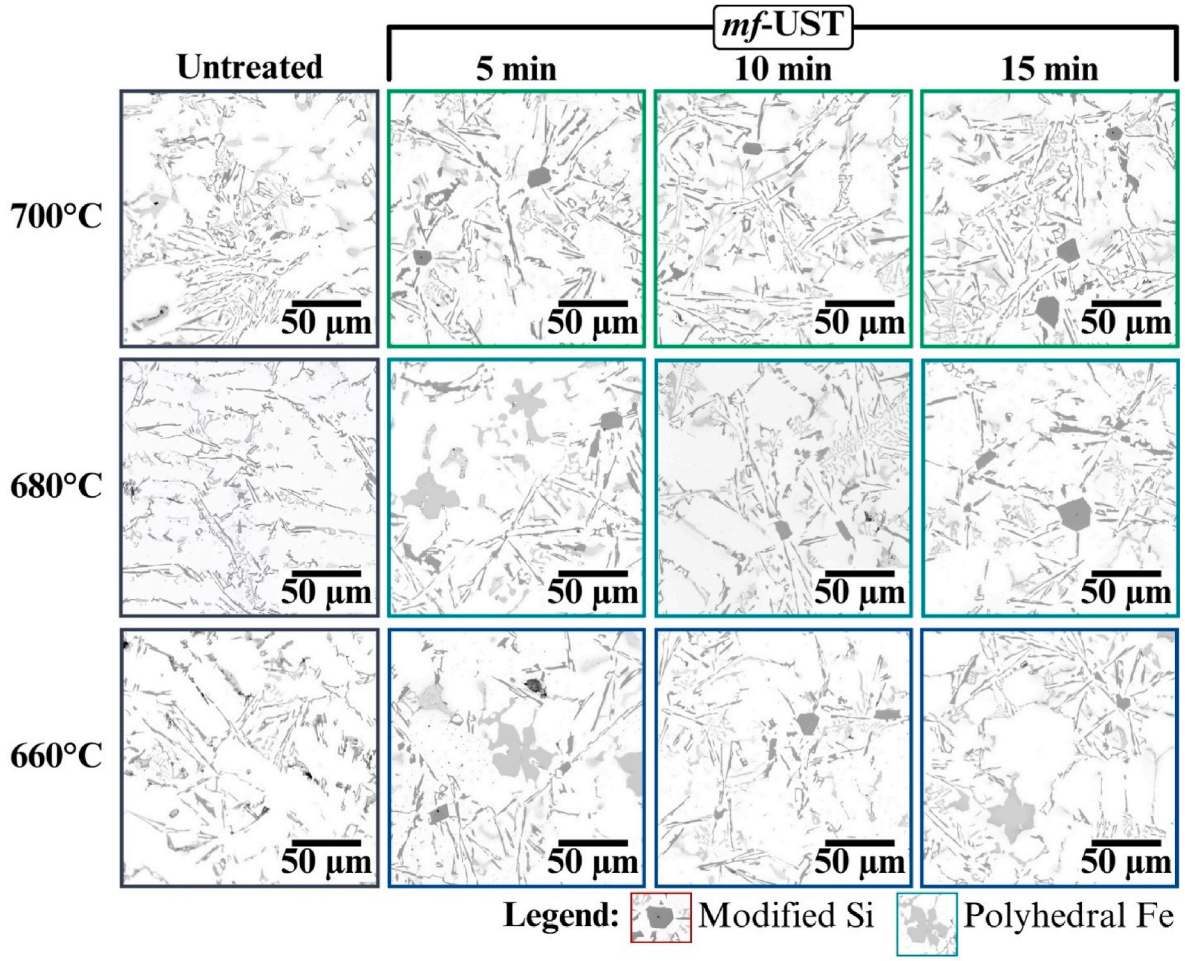


Fig. 4. OM images of A380 samples at three processing temperatures across different treatment times. *Rows from top to bottom:* 700 °C, 680 °C, and 660 °C. *Columns from left to right:* untreated reference, and *mf*-UST treated for 5 min, 10 min, and 15 min. Examples of modified Si and polyhedral Fe-phase are highlighted in the legend below the table. Scale bar = 50 µm.

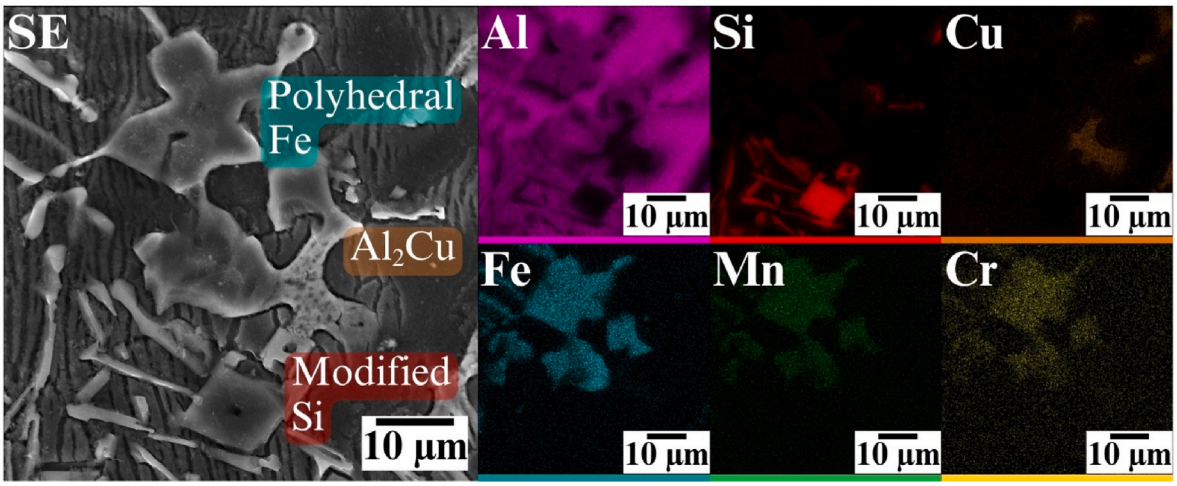


Fig. 5. SEM micrographs of an etched sample treated with *mf*-UST for 5 min at 680 °C displaying three major intermetallic phase morphologies. Scale bar = 10 μm.

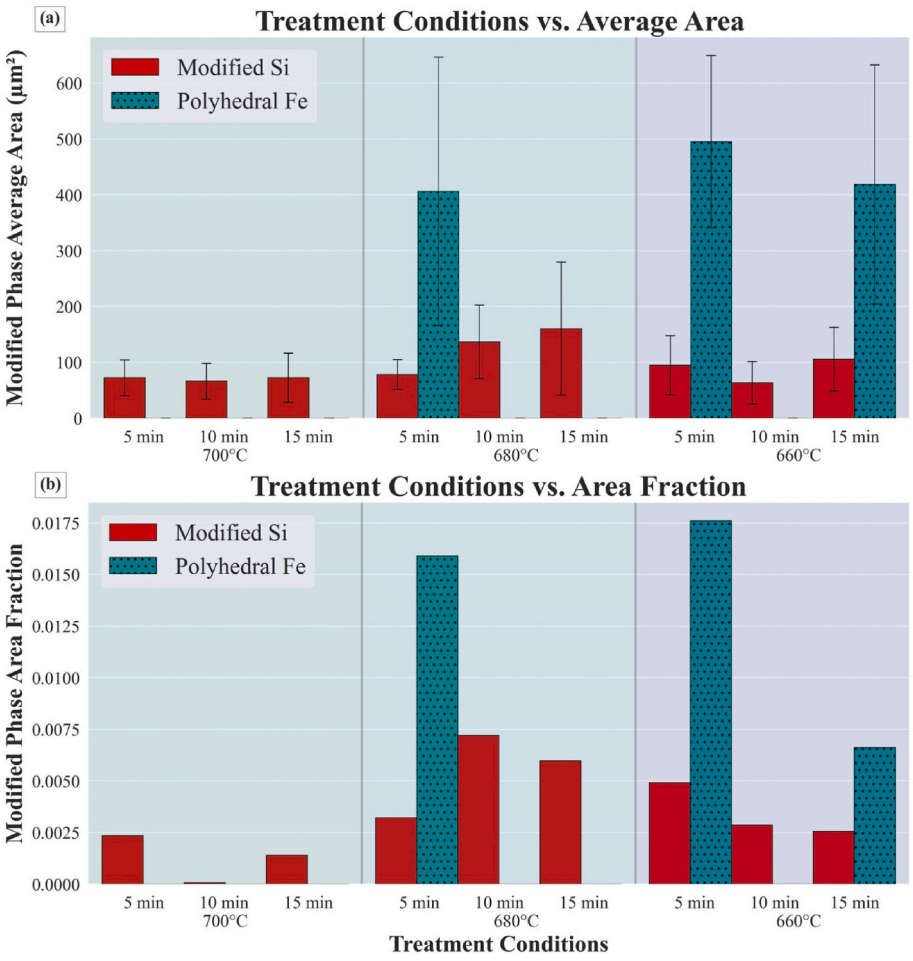


Fig. 6. Bar graphs of modified phase morphologies blocky-Si (red, solid) and polyhedral Fe-intermetallic (teal, dotted) (a) average area and (b) area fraction for all *mf*-UST temperature and time samples. (For interpretation of the references to colour in this figure legend, the reader is referred to the Web version of this article.)

and Al_2Cu is the last phase that forms. Although Thermo-Calc predicts the formation of β-Al_5FeSi, the untreated microstructure of A380 does not display the traditional needle-like morphology of this phase. Instead the untreated microstructures contain script-like α-$Al_{15}(Fe, Mn)_3Si_2$ morphology which is unexpected at a Fe/Mn ratio of 0.859:0.201, but is likely due to the Cr content (Table 1) [3,4].

Thermal analysis data collected for untreated and *mf*-UST samples treated for 5 min, validate the observed grain refinement and a new Fe-intermetallic phase morphology, Fig. 12. The untreated A380 temperature vs. time curve follows the predicted Scheil curve closely. An enlargement of the first plateau within the temperature vs. time curve shows a liquidus temperature of approximately 583 °C with a significant 3 °C undercooling in the untreated sample, minimized 1 °C undercooling in the 700 °C, and relatively no undercooling with a new peak in the

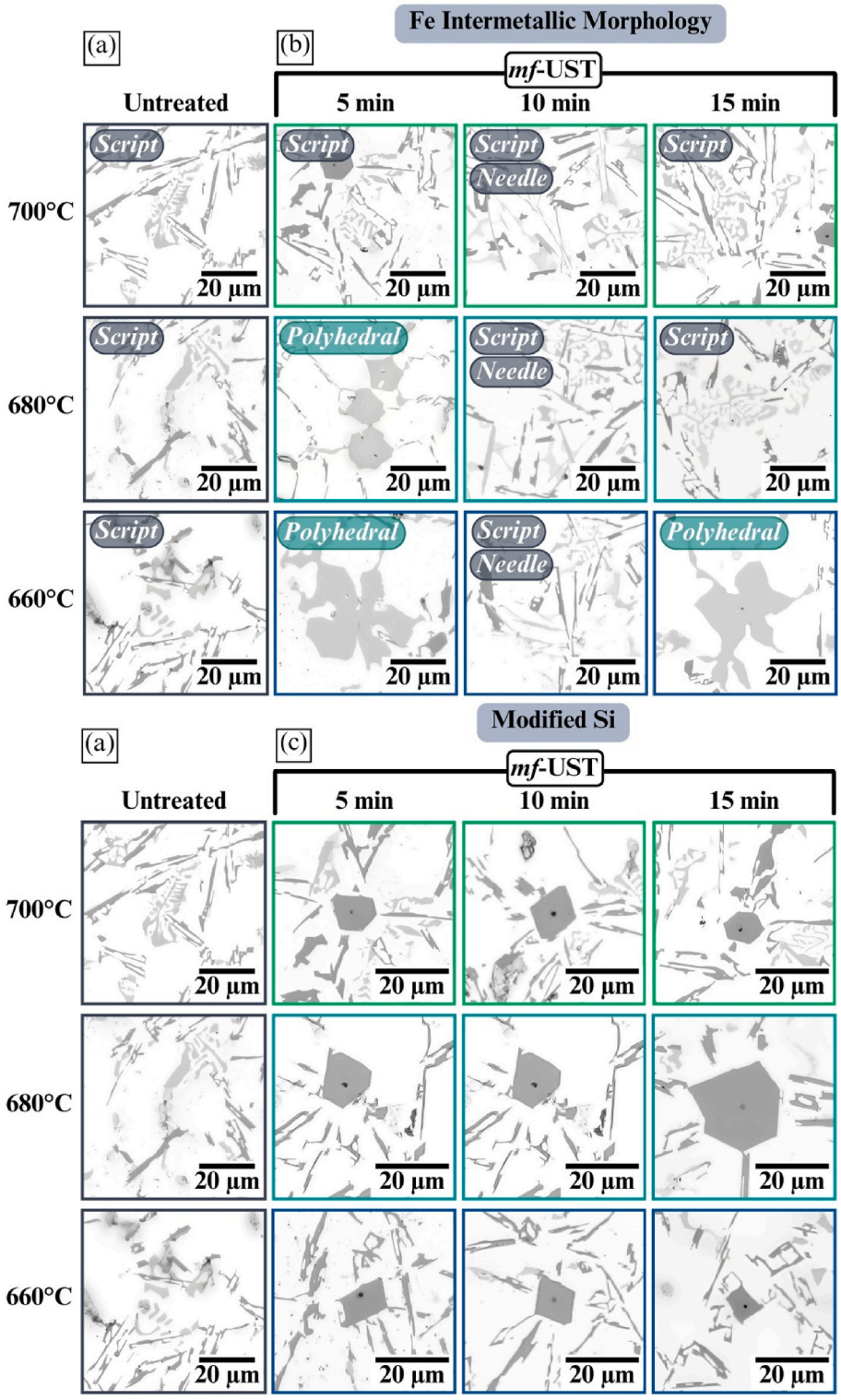


Fig. 7. Optical micrographs comparing (a) untreated microstructures to (b) the variation in the morphology of Fe-intermetallics with treatment temperature and duration, and blocky-Si with pores found throughout all *mf*-UST temperature and time samples.

680 °C and 660 °C, Fig. 12(b and c). An enlargement of the cooling rate vs. time, Fig. 12(e), reveals an additional thermal event preceding primary aluminum solidification, temporally consistent with the appearance of the polyhedral Fe-rich morphology seen at 680 °C and 660 °C with two peaks compared to one in the untreated sample. No changes were observed along other points of the curve such as at the eutectic Si formation temperature of 565 °C nor at the Al_2Cu formation temperature of approximately 500 °C. The key finding from the thermal analysis results is the correlation between samples with the least amount of undercooling before Al formation and a new peak ahead of Al solidification, seen in samples treated with *mf*-UST for 5 min at 680 °C and 660 °C. The microstructures of these samples reflect this observation, i.e. the highest degree of grain refinement (Fig. 3) is achieved in samples with formation of the polyhedral Fe-intermetallic phase (Fig. 7).

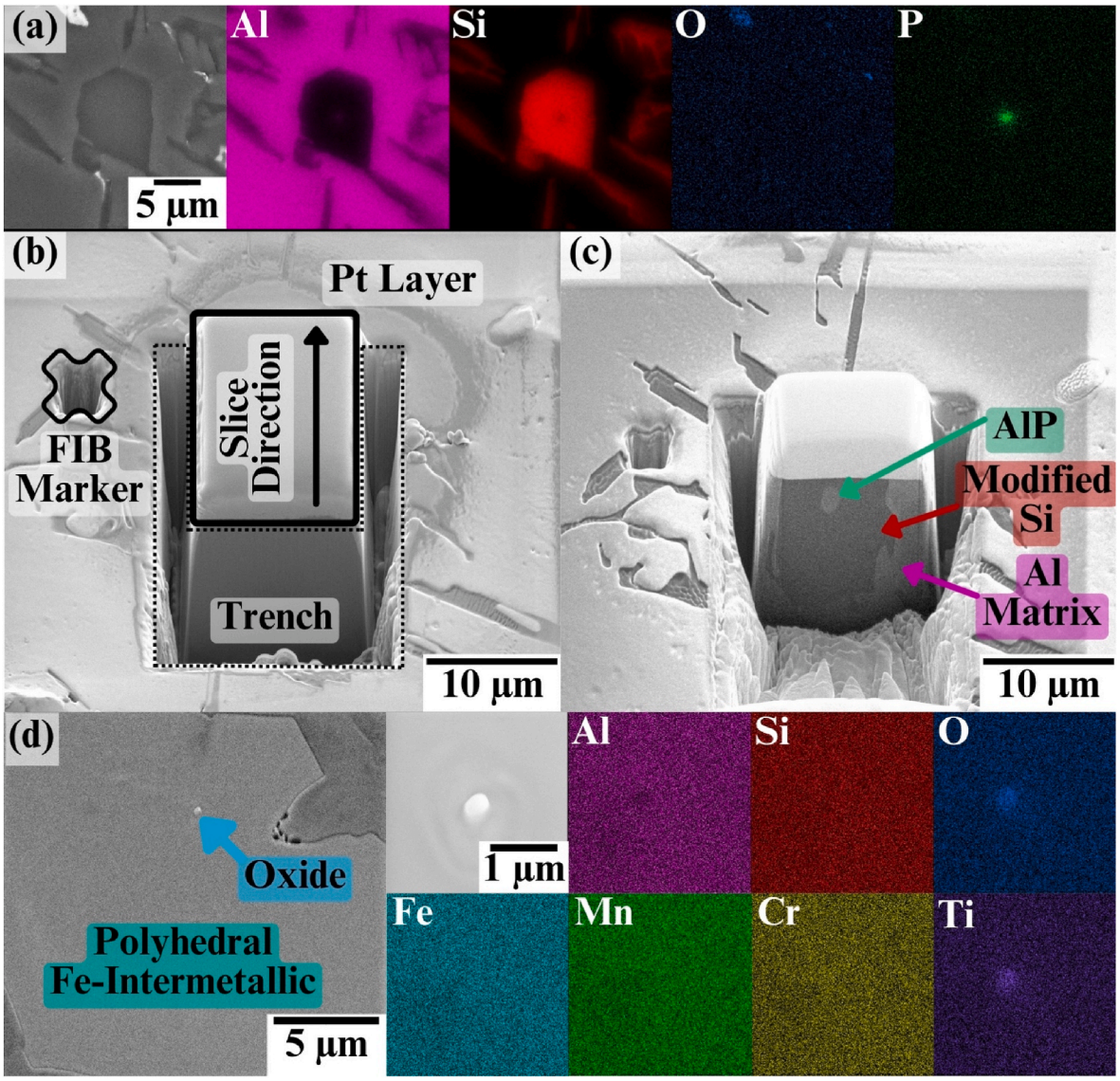


Fig. 8. SEM-EDS of sample treated with *mf*-UST for 5 min at 680 °C, (a) modified Si with AlP signal below the surface, (b) SEM serial sectioning setup, and (c) cross-section reveal of the AlP particle, (d) SEM-EDS of polyhedral Fe-intermetallic phase and FIB revealed particle with EDS signal of Ti and O.

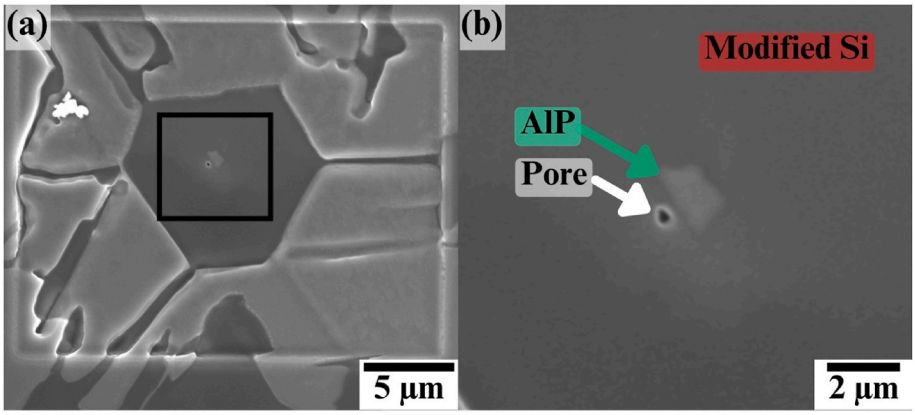


Fig. 9. (a) Micrograph of SEM-FIB erosion of modified Si revealing a pore and an AlP particle at the center, enlarged and labeled in (b).

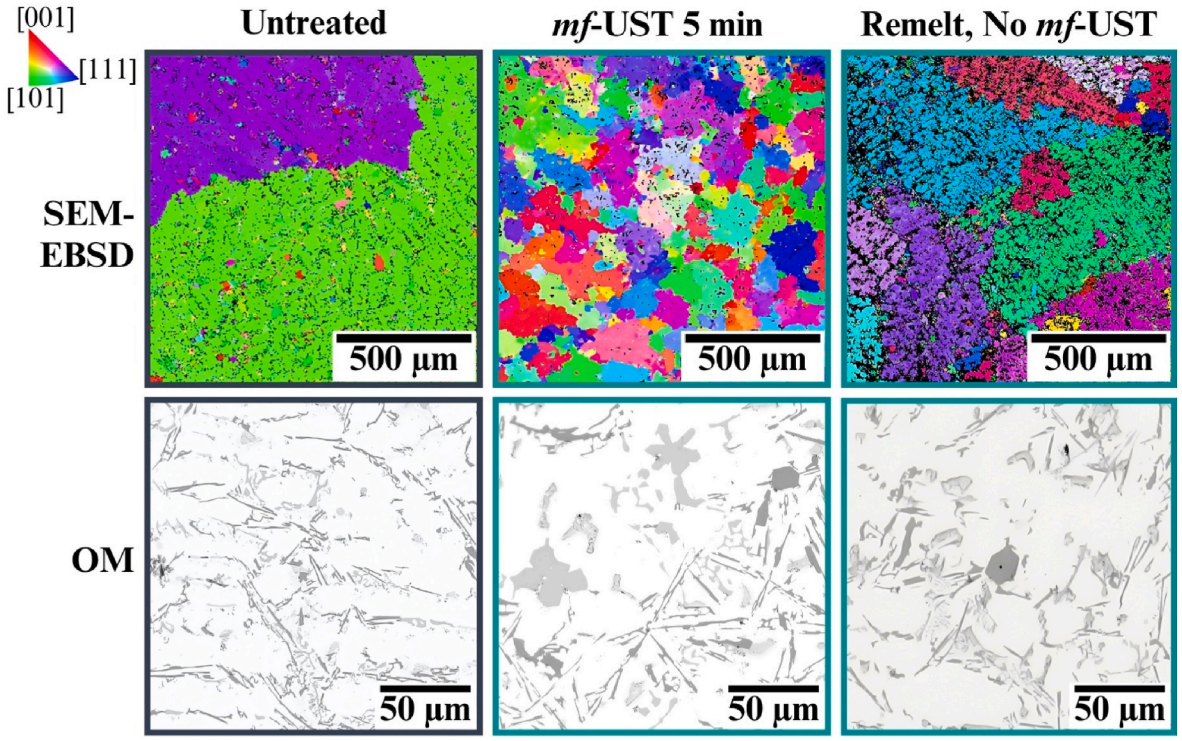


Fig. 10. SEM-EBSD (top row) and optical micrographs (bottom row) of A380 cast at 680 °C untreated, with 5 min of *mf*-UST, and remelted without *mf*-UST.

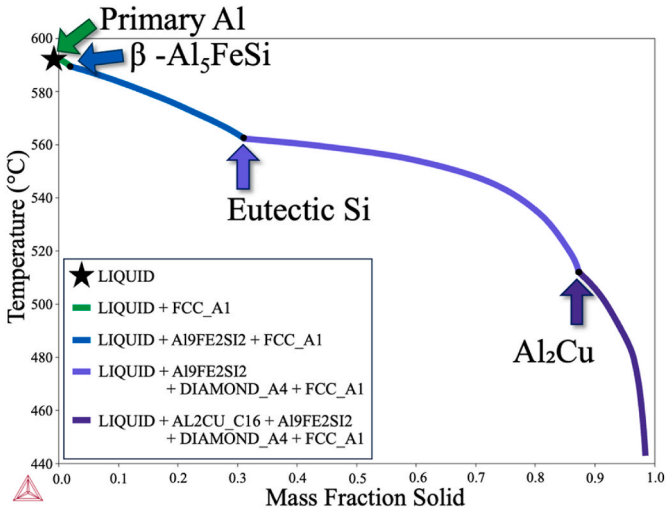


Fig. 11. Temperature vs. mass fraction solid Scheil solidification curve for commercial A380 generated by thermodynamic simulation in Thermo-Calc (note that β-Al_5FeSi phase formation is predicted to occur around 0.012 mass fraction solid).

4. Discussion

4.1. Evidence for mf-UST modified phase morphologies

Compared to untreated A380, *mf*-UST samples displayed three modified phase morphologies: blocky-Si, polyhedral Fe-intermetallic, and a needle-like phase reminiscent of β-Al_5FeSi (Fig. 7). Blocky-Si appeared in treated samples across all processing conditions. At the center of many of these phases a 'pore' was observed in the cross-sections, which was determined to be an artifact of an AlP particle via SEM-EDS and serial sectioning. In some cases, however, a separate pore was found attached to the AlP (Fig. 9) when revealed using FIB serial sectioning. The cavities may be associated with gas entrapment or particle pull-out. Their specific origin cannot be resolved from the present observations. It is likely that these pores are bubbles produced by ultrasonic energy around trapped hydrogen. These bubbles did not complete their cavitation cycle once sonification was terminated, and survived during solidification [31]. During *mf*-UST treatment, AlP particles fragment, while simultaneously producing cavitation bubbles on the AlP particle surfaces.

The modified Si in the *mf*-UST treated samples does not have the expected morphology of the Si phase we observe in hypoeutectic alloys of the Al-Si system. Rather, the modified Si in the *mf*-UST treated samples has the same morphology as the primary Si observed in hypereutectic Al-Si systems (>12.6% Si) [32–34]. It is possible that this phase is an alternate morphology that forms during the eutectic formation, however this difference is undetected in the thermal analysis data. The alternative is that this phase forms early in solidification, at a temperature higher than the data collected in thermal analysis explaining why it remains as a permanent artifact and survives remelting. Two factors have been proposed as contributing to the formation of modified Si either individually or in combination: 1) the potency of trace P (~0.001 wt%) is increased by *mf*-UST, and/or 2) cavitation undercooling.

AlP is a known nucleant of primary Si in hypereutectic Al-Si alloys due to the primary solidification and coherency between AlP and Si [34–36]. It has also been shown that hypoeutectic Al-Si alloys can form this phase morphology. The presence of AlP changes the solidification sequence and modifies the eutectic morphology [35]. AlP is known to be poisoned by minor alloying elements such as Na which is equally present in A380 (Table 1) [35,37]. *mf*-UST most likely diminishes the poisoning effect of other eutectic Si modifiers (Na, Ca, Sr, etc.) on P, which in turn increases the potency of AlP with *mf*-UST. Ultrasonic treatment potentially enhances the wettability [38] of trace AlP particles and fragments them to a preferential size for nucleation of Si. The repeated association of AlP-containing particles with blocky Si suggests that UST may facilitate particle fragmentation, redistribution, exposure, and/or interfacial contact. Normally wettability is not an issue when particles are

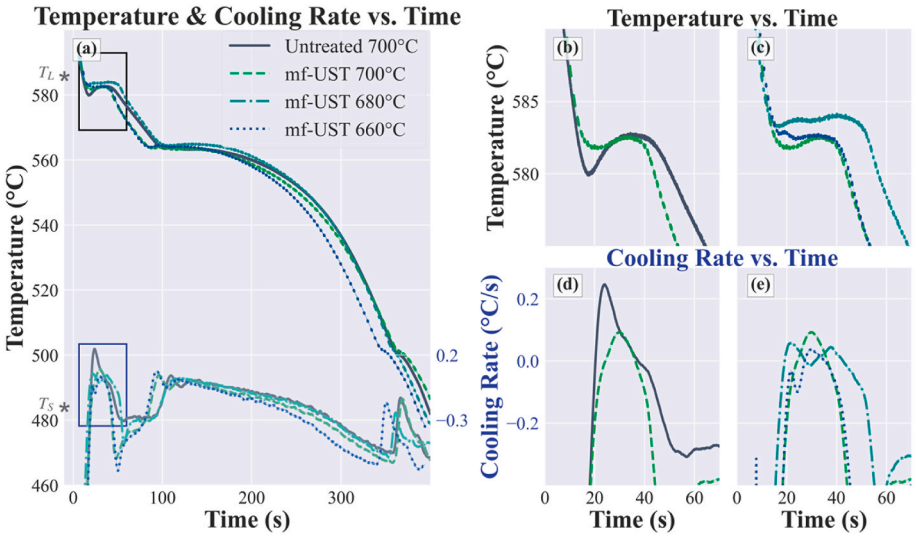


Fig. 12. (a) Thermal analysis temperature (°C) and cooling rate (°C/s) vs. time (s) curves for untreated at 700 °C (solid gray), *mf*-UST 5 min at 700 °C (dashed green), 680 °C (dash-dot teal), and 660 °C (dotted blue) marked with T_L, liquidus, and T_S, solidus temperatures. (b) Enlargement of the first phase formations boxed in (a) for with/without *mf*-UST at 700 °C, and (c) all *mf*-UST samples. (d), (e) Respective cooling rate vs. time for (b) and (c). (For interpretation of the references to colour in this figure legend, the reader is referred to the Web version of this article.)

precipitated out in a liquid due to the increase in surface energy. The present data does not distinguish between deagglomeration, improved wetting or changes in local solute conditions. The appearance of P in Al casting alloys is traditionally a contaminant, especially in secondary Al as the content increases with additional remelts (foundry crucibles/equipment, master alloy/refiner additions, scrapyard contamination, etc.). P as a contaminant has a negative impact on the mechanical strength of the alloy because it reacts with Si modifiers and diminishes their refining impact as well as acting as a defect for crack propagation [39]. The ability of mf-UST to convert trace P from a contaminant to a refining agent is most valuable in the recovery of secondary Al by not only maintaining but increasing mechanical strength.

Cavitation undercooling is the theory that cavitation bubbles exert a pressure on the liquid which reduces the local liquidus temperature and provides a surface for heterogeneous nucleation [20,30,40]. It is suspected that cavitation undercooling resulted in *mf*-UST-induced solute redistribution producing regions of local chemical heterogeneities which contribute to the observed changes in solidification behavior. Hypereutectic-reminiscent blocky-Si formation has been observed in hypoeutectic Al-Si alloys with traditional UST, and the attributed mechanism is cavitation undercooling [41]. The composition of the matrix near primary Si is notably higher in Si compared to the untreated material (Supplemental: Table 1). Normally, the matrix near a phase will have a lower content of the respective composition of the depleted zone phase [30]. In this case, there is a higher content of Si, indicating that the phase may have formed in a local hypereutectic region. In this study, the combination of a coherent nuclei and a local hypereutectic composition produced by cavitation undercooling contributed to the formation of modified phase morphologies via an altered solidification chronology.

Similar conditions are required for the formation of the polyhedral Fe-intermetallic phase, except that the nuclei are in the form of titanium oxide. There is a strong dependence of this phase stability with temperature where it strictly forms at temperatures 680 °C or lower. There is also a dependence of this phase stability with treatment time, where titanium oxide nucleates polyhedral Fe-intermetallic with 5 min of *mf*-UST and sometimes with 15 min (Fig. 7(b)). Previous studies have shown that AlP is a nucleant of β-Al_5FeSi [42,43]. It is predicted that the preference of titanium oxide and AlP oscillates with changing *mf*-UST processing time as seen in the alternating morphologies from polyhedral Fe-intermetallic to β-Al_5FeSi.

4.2. Proposed particle-mediated nucleation pathway

The cavitation threshold determines the onset of cavitation bubble development and collapse, which is dependent on extrinsic factors such as the viscosity, trapped gases, particles, and energy input [5]. This acoustic pressure value has been reported in the range of 100 W/cm^2 [25,44]. Factors that reduce the cavitation threshold include temperature, hydrogen content, particle inclusions such as oxides, and a stabilized frequency output uniformly treating the melt volume. The *mf*-UST utilized in this study was determined to meet the cavitation threshold with significant acoustic pressure and acoustic intensity. Acoustic pressure (p) applied by cavitation during *mf*-UST can be estimated by Eq. (1) where ρ is the density of liquid Al, c is the speed of sound in liquid Al, ϖ is the angular frequency, ($2\pi f$), and A is the node-to-peak amplitude. Acoustic pressure can be related to acoustic intensity as shown by Eq. (2). Using the density of liquid A380 at 700 °C [45], $\rho = 2485.2$ kg/m^3, respective speed of sound [46] $c = 4600$ m/s, average frequency of our experiment $f = 20$ kHz, and approximate peak-to-peak amplitude of 10 μm, $A = 5$ μm, the estimated experimental acoustic pressure is 7.18 MPa and acoustic intensity is 450 W/cm^2. Comparing this with 660 °C where the density and speed of sound both increases, the acoustic pressure and intensity would be expected to increase as well, confirming that all experiments were conducted above the cavitation threshold.

$$p = \rho\, c \varpi\, A \tag{1}$$

$$I = \frac{p^2}{\rho c} \tag{2}$$

An important mechanism behind liquid-state *mf*-UST grain refinement is that when bubbles form and expand due to cavitation, they create small zones of high pressure around them [5,16,20,22]. When the pressure around the liquid increases the local melting temperature also increases, in accordance with the Clapeyron relation, Eq. (3),

$$\frac{dP}{dT} = \left(\frac{\Delta H}{T_m \Delta V}\right) \tag{3}$$

where P is pressure, ΔH is the change in enthalpy, ΔV is the change in volume, T_m is the liquidus temperature, and T is the temperature. Pressures of this magnitude (greater than 7 MPa) causes local undercooling. This undercooling allows solid nuclei to start forming on the

surface of the bubble, functioning as sites for heterogeneous nucleation, i.e. cavitation-enhanced heterogeneous nucleation [6,16,19,20]. When *mf*-UST is continuously applied above the cavitation threshold, bubbles continuously collapse [10]. Once the ultrasonic power is stopped, the bubbles that survive due to their size, are likely the ones observed attached to AlP nuclei within the modified Si phase.

4.3. Dependence of grain refinement on phase modification

Existing literature in the field states that liquid-state grain refinement relies on the deagglomeration and distribution of solid oxides via UST which enhance nucleation for Al grains [5,8,23,47–49]. Also considered is the possibility of cavitation bubbles themselves providing high pressure and surfaces for the undercooling and nucleation of primary Al [5,16,20,22]. The results of this study show that *mf*-UST conditions affect grain refinement and modify the microstructure. Fig. 3 shows that optimal grain refinement is predicted at a temperature between 680 °C and 660 °C with 5 min of treatment as well as with 15 min of treatment. Two different trends are observed when *mf*-UST processing is carried out at different treatment temperatures. For the 700 °C treated samples, average grain size trends consistently downward from the untreated value of 776 μm to 193 μm after 15 min of *mf*-UST. Meanwhile, for the 680 °C and 660 °C treated samples the average grain size fluctuates from the lowest values of 110 μm, 180 μm with 5 min of UST, increases to 395 μm, 296 μm with 10 min, and decreases to 289 μm, 173 μm with 15 min of *mf*-UST, respectively. The trend for the 700 °C follows what is expected in *mf*-UST grain refinement via oxide deagglomeration for heterogeneous nucleation. In this case, longer treatment times are more effective for the break-up and distribution of solid oxides that exist in the melt, meaning that the highest level of grain refinement can be attained with longer treatment. In the case of 680 °C and 660 °C it is likely that *mf*-UST grain refinement is reliant on a combination of two mechanisms: 1) oxide break-up; and 2) modified phase morphologies.

For the 660 and 680 °C *mf*-UST treated samples, at 5 min, the morphology of the Fe-intermetallics observed are script-like and polyhedral; at 10 min it is script-like and needle-like; at 15 min it reverts back to the polyhedral morphology for 660 °C processing temperature, and for 680 °C, script-like (Figs. 7(b) and 13). The fluctuation in Fe-phase morphology is mirrored by the fluctuation observed in average grain size. The results of this study indicate a dependence of grain refinement on intermetallic phase morphology. The polyhedral Fe-intermetallic, where present, has been shown to form first in the thermal analysis data with an early peak before the Al matrix (Fig. 12(c)). Its formation before primary aluminum and its spatial association with starburst aluminum growth make it a plausible intermediate substrate for α-Al nucleation, influencing the first major drop in average grain size with 5 min of *mf*-UST at 680 °C and 660 °C. After 10 min of treatment, the Fe-intermetallic morphology has modified to script-like and needle-like which are both morphologies known to form after primary Al (Fig. 11) [3,25]. In this case, the mechanism for grain refinement relies solely on oxide break-up. After 15 min of treatment the 680 °C sample contains script-like morphology, meaning the mechanism at play is oxide break-up. In 15 min samples treated at 660 °C the polyhedral Fe-intermetallic morphology is operative, and the mechanisms for grain refinement are reliant on Fe-intermetallic phase morphology as well as oxide break-up. In the 700 °C sample the morphology fluctuates from α-script, to α-script and β-platelet, and back to α-script with 5, 10, and 15 min of treatment respectively, Fig. 13. Under these conditions there was no formation of polyhedral Fe-intermetallic, thus the oxide break-up mechanism is operative (see Fig. 14).

An additional mechanism at play is the survival of nuclei under certain processing conditions. The morphology of the Fe-intermetallic phase is likely connected to the stability of the titanium oxide nuclei. The polyhedral Fe-rich morphology associated with Ti-O-containing particles was only detected at treatment temperatures of 680 °C or below, seen via the microstructures and thermal analysis data (Figs. 7(b) and 13). There is a connection between the presence of certain Fe-intermetallic morphologies and smaller grain size. It is suspected that when titanium oxide loses stability and can no longer provide a nucleation site, that AlP nucleates the β-platelet morphology. Previous studies have reported that the addition of P to Al-Si-Cu alloys results in the nucleation of the β-platelet morphology [42,43]. Oddly, the β-platelet morphology is not nucleated by AlP in all samples, but only when the polyhedral morphology is not present.

An interesting feature of *mf*-UST is that there is a persistent effect after one remelting cycle on nucleation sites. For example, when previously treated samples are cast, remelted, and cast again without *mf*-UST they display modified Si morphology and minor grain refinement when compared to commercial ingots (Fig. 10). This is indication that the increased potency of AlP particles is effective upon recasting and

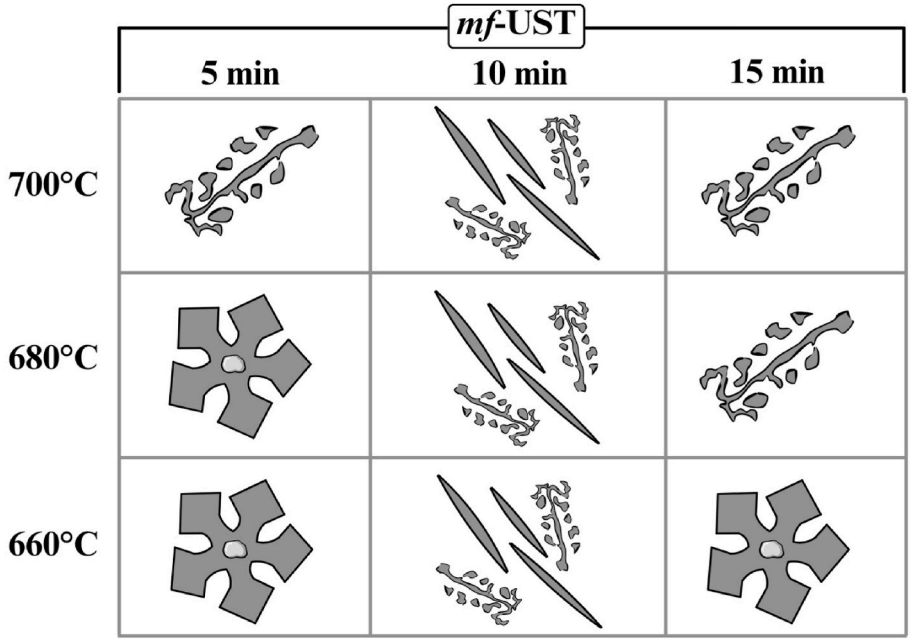


Fig. 13. Map of Fe-intermetallic phase formations with varying *mf*-UST time and temperature.

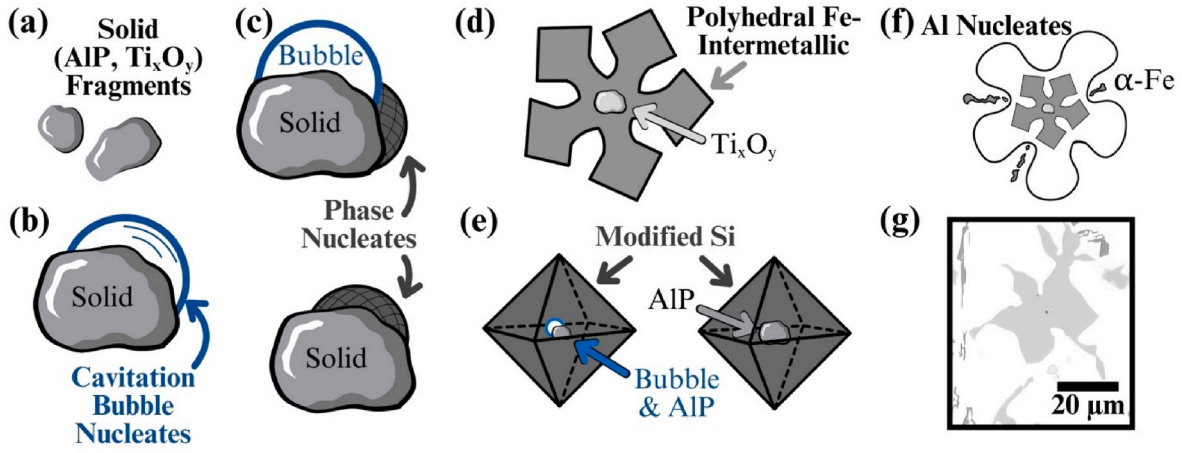


Fig. 14. Proposed mechanistic framework for particle-mediated phase selection and grain refinement. (a) Solid particles (AlP and Ti_xO_y) are fragmented via UST, (b) a cavitation bubble attaches to the fragmented particles, (c) modified phases nucleate on the surface of the fragmented particles (d) polyhedral Fe-intermetallic nucleates on Ti_xO_y, (e) modified Si nucleates on AlP and AlP/bubble combinations, (f) faceted polyhedral morphology enhances the nucleation of Al grains resulting in a star-burst microstructural pattern, as seen in (g) optical micrograph.

potentially it applies for other nuclei that are responsible for Al grain refinement via *mf*-UST.

5. Conclusions

In this study, we found direct evidence of AlP, AlP/pore combinations within modified blocky-Si and titanium oxide within polyhedral Fe-intermetallic. Two phases, Si-phase and Fe-intermetallic phase, experienced modification to their morphologies and the Fe-intermetallic phase alternated between primary and secondary solidification pathways. A correlation between modified Fe-intermetallic morphology and grain refinement was observed. The main conclusions of this study are: 1) Liquid-state *mf*-UST changes the expected phase formation via nuclei break-up, cavitation undercooling, and local hypereutectic regions. 2) Liquid-state *mf*-UST increases the potency of trace elements (~0.001 wt %) to function as nuclei for phase modification and grain refinement. The ability of *mf*-UST to target trace elements and convert their existence from contaminants/defects to potential strength-enhancing grain refiners has much value in the application of this processing method for Al recycling and secondary Al production. The maximum observed refinement was found within 5 min of *mf*-UST at 680 °C displaying an 85.8% reduction in grain size. 3) Modified Fe-intermetallic phase morphologies provide heterogeneous nucleation sites for Al in addition to distributed oxide nuclei that influence grain refinement. The Fe-intermetallic phase morphology can be tailored by varying treatment time. 4) The effects of *mf*-UST are semi-permanent, observed in remelted, previously treated material which shows retention of notable grain refinement and phase modification without additional treatment. Future study on varying trace element content and TEM-investigation of the Fe-intermetallic atomic structure will be necessary to pursue this work further.

CRediT authorship contribution statement

Raquel F. Jaime: Writing – review & editing, Writing – original draft, Visualization, Validation, Methodology, Investigation, Formal analysis, Data curation, Conceptualization. **Andrew Y. Zang:** Writing – review & editing, Formal analysis, Data curation. **Adrianne Chang:** Methodology, Investigation, Formal analysis, Data curation. **Carl Söderhjelm:** Writing – review & editing, Supervision, Project administration, Methodology, Investigation, Formal analysis, Conceptualization. **Hélder Puga:** Writing – review & editing, Validation, Supervision, Resources, Project administration, Methodology, Investigation, Formal analysis, Conceptualization. **Diran Apelian:** Writing – review & editing, Validation, Supervision, Resources, Project administration, Methodology, Investigation, Funding acquisition, Formal analysis, Conceptualization.

Declaration of competing interest

The authors declare that they have no known competing financial interests or personal relationships that could have appeared to influence the work reported in this paper.

Acknowledgements

The authors gratefully acknowledge funding from the Advanced Casting Research Center (ACRC), and especially the chair of the focus group of this project, Mr. Martijn Vos. Special thanks to MPI Ultrasonics for their assistance regarding Multifrequency, Multimode, Modulated Sonic & Ultrasonic Vibrations technology, and our thanks for support received from Dr. Miodrag Prokic. The authors acknowledge strategic partnerships with AMETEK, Buehler, Evident Scientific, Inductotherm, Solutions Fonderie, EMC Hycal, and VJT. The authors wish to thank Ana Sofia Diaz Santos, Landon Renaud, and Eric Lehman for their assistance in the laboratory and Dr. Ich Tran for microscopy assistance. The authors acknowledge the use of facilities and instrumentation at the UC Irvine Materials Research Institute (IMRI), which is supported in part by the National Science Foundation through the UC Irvine Materials Research Science and Engineering Center (DMR-2011967).

Appendix A. Supplementary data

Supplementary data to this article can be found online at https://doi.org/10.1016/j.msea.2026.151104.

Data availability

Data will be made available on request.

References

[1] S. Ahmad, J. Steen, T. Zajac, M. Azadi, S.H. Ali, Carbon emissions in metal manufacturing productivity: a global analysis of aluminium smelting, Energy Res. Social Sci. 129 (2025) 104343.
[2] S. Jones, C. Mitchell, The Impact of the Bauxite Boom on People and Planet, Mighty Earth, 2024.

[3] E. Cinkilic, C.D. Ridgeway, X. Yan, A.A. Luo, A formation map of iron-containing intermetallic phases in recycled cast aluminum alloys, Metall. Mater. Trans. A 50 (2019) 5945–5956.
[4] S.G. Shabestari, The effect of iron and manganese on the formation of intermetallic compounds in aluminum–silicon alloys, Mater. Sci. Eng. A 383 (2004) 289–298.
[5] G. Eskin, D. Eskin, Ultrasonic Treatment of Light Alloy Melts, 2014, https://doi.org/10.1201/b17270.
[6] H. Puga, S.D. Tohidi, V.H. Carneiro, J. Meireles, M. Prokic, Ceramic sonotrodes for light alloy melt treatment, Int. J. Met. 15 (2021) 459–469.
[7] C.J. Todaro, et al., The effect of ultrasonic melt treatment on macro-segregation and peritectic transformation in an Al-19Si-4Fe alloy, Metall. Mater. Trans. A 48 (2017) 5579–5590.
[8] R.F. Jaime, H. Puga, M. Prokic, C. Söderhjelm, D. Apelian, Fundamentals of ultrasonic treatment of aluminum alloys, Int. J. Met. (2024) 1–25, https://doi.org/10.1007/s40962-023-01253-w.
[9] J. Mondal, R. Lakkaraju, P. Ghosh, M. Ashokkumar, Acoustic cavitation-induced shear: a mini-review, Biophys. Rev. 13 (2021) 1229–1243.
[10] T. Thanh Nguyen, Y. Asakura, S. Koda, K. Yasuda, Dependence of cavitation, chemical effect, and mechanical effect thresholds on ultrasonic frequency, Ultrason. Sonochem. 39 (2017) 301–306.
[11] C.E. Brennen, Cavitation and Bubble Dynamics, Oxford University Press, Pasadena California, 1995.
[12] D. Zhang, et al., Multi-frequency therapeutic ultrasound: a review, Ultrason. Sonochem. 100 (2023) 106608.
[13] P. Miodrag, Multifrequency Ultrasonic Structural Actuators, 2002.
[14] V.S. Moholkar, S. Rekveld, M.M.C.G. Warmoeskerken, Modeling of the acoustic pressure fields and the distribution of the cavitation phenomena in a dual frequency sonic processor, Ultrasonics 38 (2000) 666–670.
[15] G. Servant, J.L. Laborde, A. Hita, J.P. Caltagirone, A. Gérard, On the interaction between ultrasound waves and bubble clouds in mono- and dual-frequency sonoreactors, Ultrason. Sonochem. 10 (2003) 347–355.
[16] H. Puga, S. Costa, J. Barbosa, S. Ribeiro, M. Prokic, Influence of ultrasonic melt treatment on microstructure and mechanical properties of AlSi9Cu3 alloy, J. Mater. Process. Technol. 211 (2011) 1729–1735.
[17] F. Wang, I. Tzanakis, D. Eskin, J. Mi, T. Connolley, In situ observation of ultrasonic cavitation-induced fragmentation of the primary crystals formed in Al alloys, Ultrason. Sonochem. 39 (2017) 66–76.
[18] S. Wang, Z.P. Guo, X.P. Zhang, A. Zhang, J.W. Kang, On the mechanism of dendritic fragmentation by ultrasound induced cavitation, Ultrason. Sonochem. 51 (2019) 160–165.
[19] H. Puga, J. Barbosa, V.H. Carneiro, F.V. Barbosa, J.C. Teixeira, Optimizing high-volume ultrasonic melt degassing using synchronized kinematic translation, J. Mater. Res. Technol. 14 (2021) 2832–2844.
[20] H. Puga, et al., Influence of indirect ultrasonic vibration on the microstructure and mechanical behavior of Al–Si–Cu alloy, Mater. Sci. Eng. A 560 (2013) 589–595.
[21] S. Wang, J. Kang, X. Zhang, Z. Guo, A study on the effect of ultrasonic treatment on the microstructure of Sn-30 wt.% Bi alloy, Materials 11 (2018) 1870.
[22] T.V. Atamanenko, D.G. Eskin, L. Zhang, L. Katgerman, Criteria of grain refinement induced by ultrasonic melt treatment of aluminum alloys containing Zr and Ti, Metall. Mater. Trans. A 41 (2010) 2056–2066.
[23] F. Wang, et al., A refining mechanism of primary Al3Ti intermetallic particles by ultrasonic treatment in the liquid state, Acta Mater. 116 (2016) 354–363.
[24] C.M. Dinnis, J.A. Taylor, A.K. Dahle, As-cast morphology of iron-intermetallics in Al–Si foundry alloys, Scr. Mater. 53 (2005) 955–958.
[25] J.A. Taylor, Iron-containing intermetallic phases in Al-Si based casting alloys, Procedia Mater. Sci. 1 (2012) 19–33.
[26] M. Prokic, MMM technology | MPI ultrasonics - Sonic and ultrasonic processing technology, MPI Ultrasonics (2001). https://www.mpi-ultrasonics.com/.
[27] K. Xiang, et al., Operando study of the dynamic evolution of multiple Fe-rich intermetallics of an Al recycled alloy in solidification by synchrotron X-ray and machine learning, Acta Mater. 279 (2024) 120267.
[28] H. Becker, T. Bergh, P.E. Vullum, A. Leineweber, Y. Li, Effect of Mn and cooling rates on α-, β- and δ-Al–Fe–Si intermetallic phase formation in a secondary Al–Si alloy, Materialia 5 (2019) 100198.
[29] J. Roger, F. Bosselet, J.C. Viala, X-rays structural analysis and thermal stability studies of the ternary compound α-AlFeSi, J. Solid State Chem. 184 (2011) 1120–1128.
[30] L. Zhang, S. Chen, Q. Li, G. Chang, Formation mechanism and conditions of fine primary silicon being uniformly distributed on single αAl matrix in Al-Si alloys, Mater. Des. 193 (2020) 108853.
[31] K. Pericleous, V. Bojarevics, C. Tonry, Contactless ultrasonic cavitation in alloy melts. https://doi.org/10.3390/ma12213610, 2019 https://doi.org/10.3390/ma12213610.
[32] C.L. Xu, H.Y. Wang, C. Liu, Q.C. Jiang, Growth of octahedral primary silicon in cast hypereutectic Al–Si alloys, J. Cryst. Growth 291 (2006) 540–547.
[33] Y. Xu, et al., Revealing the nucleation kinetics of primary Si particles in hypereutectic Al–Si alloys under the influence of P inoculation, J. Mater. Sci. 55 (2020) 15621–15635.
[34] J. Li, F.S. Hage, X. Liu, Q. Ramasse, P. Schumacher, Revealing heterogeneous nucleation of primary Si and eutectic Si by AlP in hypereutectic Al-Si alloys, Sci. Rep. 6 (2016) 25244.
[35] K. Nogita, S.D. McDonald, K. Tsujimoto, K. Yasuda, A.K. Dahle, Aluminium phosphide as a eutectic grain nucleus in hypoeutectic Al-Si alloys, J. Electron. Microsc. 53 (2004) 361–369.
[36] S.-J. Jin, et al., Refinement of Primary Si Phase in Hypereutectic Al–Si Alloy by Electrically Assisted Solidification with P Addition, Adv. Eng. Mater. 26 (2024) 2401025.
[37] A.K. Dahle, K. Nogita, S.D. McDonald, J.W. Zindel, L.M. Hogan, Eutectic nucleation and growth in hypoeutectic Al-Si alloys at different strontium levels, Metall. Mater. Trans. A 32 (2001) 949–960.
[38] J.A. Sarasua, L.R. Rubio, E. Aranzabe, J.L.V. Vilela, Energetic study of ultrasonic wettability enhancement, Ultrason. Sonochem. 79 (2021) 105768.
[39] J. Fred Major, Aluminum and aluminum alloy castings, in: S. Viswanathan, et al. (Eds.), Casting, 15 0, ASM International, 2008.
[40] L. Zhang, D.G. Eskin, L. Katgerman, Influence of ultrasonic melt treatment on the formation of primary intermetallics and related grain refinement in aluminum alloys, J. Mater. Sci. 46 (2011) 5252–5259.
[41] X. Jian, Q. Han, Formation of hypereutectic silicon particles in hypoeutectic Al-Si alloys under the influence of high-intensity ultrasonic vibration, China Found. 10 (2013) 118–123.
[42] A. Pennors, A.M. Samuel, F.H. Samuel, H.W. Doty, Precipitation of β−Al5FeSi iron intermetallic in Al-6% Si-3.5% Cu (319) type alloys: Role of Sr and P, Trans. Am. Foundrymen's Soc. 106 (1998) 251–264.
[43] L. Liu, et al., Precipitation of β-Al5FeSi phase platelets in Al-Si based casting alloys, Metall. Mater. Trans. A 40 (2009) 2457–2469.
[44] C.J. Todaro, et al., Grain structure control during metal 3D printing by high-intensity ultrasound, Nat. Commun. 11 (2020) 142.
[45] H. Cao, et al., Effect of Flow State of Pure Aluminum and A380 Alloy on Porosity of High Pressure Die Castings, Materials 12 (2019) 4219.
[46] E. Riedel, M. Liepe, S. Scharf, Simulation of ultrasonic induced cavitation and acoustic streaming in liquid and solidifying aluminum, Metals 10 (2020) 476.
[47] T.V. Atamanenko, Cavitation-Aided Grain Refinement in Aluminium Alloys, TU Delft, Delft Netherlands, 2010.
[48] D.G. Eskin, et al., Fundamental studies of ultrasonic melt processing, Ultrason. Sonochem. 52 (2019) 455–467.
[49] J. Grilo, V.H. Carneiro, J.C. Teixeira, H. Puga, Effect of ultrasonic melt treatment on solidification behavior of Al7SiMg alloy, Int. J. Met. (2022), https://doi.org/10.1007/s40962-022-00829-2, 10.1007/s40962-022-00829-2.